Passive control of flexural beam vibrations using nonlinear absorbers combined with an Acoustic Black Hole

Haiqin Li*†, Cyril Touzé*, Adrien Pelat† and François Gautier†
* *IMSIA, Institut of Mechanical Sciences and Industrial Applications, ENSTA Paris, CNRS, EDF, CEA, Institut Polytechnique de Paris, Palaiseau, France.*
† *LAUM, Laboratoire d'Acoustique de l'Université du Mans, Le Mans, France*

Summary. Acoustic Black Hole (ABH) is a new passive technique for vibration damping of thin-walled strutures such as beams and plates. It consists of a local decrease in the thickness profile, associated to the deposit of a thin viscoelastic coating in the thinnest region. One of the common feature for this technique is that it is very efficient in the high frequency range, but it is less optimal in the low frequency range. To overcome this limitation,we propose to investigate the benefit brought by different types of nonlinear dampers into the system. The effect of a Tuned Mass Damper (TMD), a Nonlinear Energy Sink, and a Bistable Nonlinear Energy Sink are respectively considered and compared. The dynamics of these systems are numerically solved using a modal approach with an energy conserving scheme. Then, by defining some frequency indicators, the low frequency performance of each aforementioned strategy is characterized. It is demonstrated that, if appropriately designed, all the proposed methods can effectively reduce the low frequency resonance peaks in the ABH structure, and hence improve the average performance of an ABH.

Introduction

The Acoustic Black Hole (ABH) effect has become an increasingly popular technique for passive noise and vibration control. Its one dimensional implementation (i.e its implementation in a beam structure) consists of a local decrease of the thickness according to a power law profile associated to the adding of a thin viscoelastic damping layer in the tapered area [1]. Existing theoretical, numerical and experimental papers show that Acoustic Black Holes induce significant localization of the bending waves, and have a strong damping effect in the middle and high frequency ranges [1]. Some design rules based on the analysis of the wave scattering induced by an ABH termination have been proposed [2] to achieve high modal damping coefficients, the underlying mechanism being interpreted using the critical coupling concept [3]. However, a significant limitation of the ABH effect leads in the fact that it is effective in the mid-high frequency range. A cut-on frequency has been defined [4], for representing the critical frequency threshold below which the ABH loses its efficiency. To overcome this issue, the idea of associating the ABH effect with some other nonlinear effects has emerged: geometrical non linearities due to vibrations with large amplitudes have been exploited [5], as well as strong nonlinearities induced by vibro-impacts [6].
In this paper, the interest of adding three different types of vibration absorbers to a beam ABH termination are tested in order to meet the requirement of a broadband passive energy mitigation. A classical tuned mass damper (TMD) is first considered, which consists of a linear device that has been proven to be a very reliable passive mitigation strategy in a large number of contexts [7, 8]. It could be awaited that once a TMD is attached to an ABH beam and tuned to one of its resonant modes below the cut-on frequency, where the ABH effect is ineffective, the peak response reduced [9], and the average perfomance of the ABH could hence be improved.
Considering the known major drawback that TMD is only effective in a narrow frequency band, a more broadband nonlinear vibration absorber consisting of an NES with cubic nonlinearity [10] is also proposed. Unlike a linear system, a unique nonlinear phenomenon called targeted energy transfer [11] could be observed for effective broadband vibration mitigation [12, 13]. A third proposition of absorber consists of a recently studied Bistable Nonlinear Energy Sink (BNES), for which the targeted energy transfer can be activated with a lower energy barrier [15, 16].
The purpose of this paper is thus to use the aforementioned three types absorbers in order to improve the performance of the ABH below its cut-on frequency, and to compare their performances. The numerical modeling of all the considered systems will be formulated in Section 2. Section 3 is mainly devoted to the numerical results, the performance of each methods will be discussed, before the conclusion given in section 4.

Equations of motion

Let us consider an ABH beam coupled to a single vibration absorber consisting in an elementary 1-DOF oscillator (see Fig. 1). The absorber is located at $x = x_c$. Its mass m is assumed to be small compared to that of the beam. It is characterized by its linear stiffness k_l, its cubic nonlinear stiffness k_n, and its damping coefficient 2σ. Considering such parameters, the three different types of absorbers can be modeled by varying k_l and k_n. More precisely, a linear TMD [7, 8] is obtained by setting $k_l > 0, k_n = 0$; while the classical NES [11] with cubic nonlinearity corresponds to the arrangement of $k_l = 0, k_n > 0$. Finally, the case of a BNES [15, 16] can be obtained for $k_l < 0, k_n > 0$.
The ABH beam is supposed to have a constant thickness h_0 in the region $x \in [0, x_{abh}]$. An ABH profile is assumed in the right hand region $x \in [x_{abh}, L]$: The thickness $h_b(x)$ is decreasing with respect to the variable x, in the form of the

power-law function

$$h_b(x) = \begin{cases} h_0, & \text{for } x \in [0, x_{abh}] \\ h_0 \left(\dfrac{x - x_{end}}{x_{abh} - x_{end}} \right)^2, & \text{for } x \in [x_{abh}, L] \end{cases} \tag{1}$$

The cross-section of the ABH beam is assumed to be rectangular and with width b, such that the cross-section area $A(x)$ and the inertia moment $I(x)$ writes respectively $A(x) = bh_b(x)$ and $I(x) = bh_b(x)^3/12$. Finally, a viscoelastic layer is added in the ABH region in consideration of ensuring the damping for a practical ABH with an inevitable truncation thickness h_t.

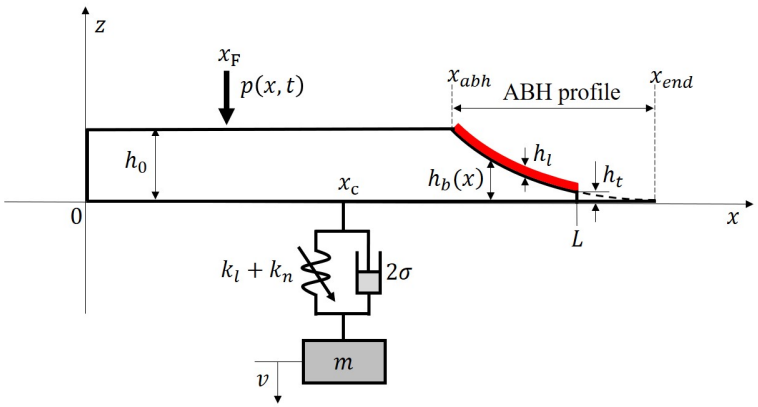

Figure 1: The layout of the considered system consists of an ABH beam coupled to a lightweight oscillator located at x_c. A thin damping layer (red) of thickness h_l is added along the ABH profile.

Let $u(x,t)$ be the transverse displacement of the beam, and $v(t)$ the motion of the absorber. The governing equation for the system can then be written as

$$\rho(x)A(x)\frac{\partial^2 u}{\partial t^2} + \frac{\partial^2}{\partial x^2}\left(D(x)\frac{\partial^2 u}{\partial x^2}\right) + f\delta(x - x_c) = p\delta(x - x_F), \tag{2a}$$

$$m\ddot{v} = f, \tag{2b}$$

$$f = k_l w + k_n w^3 + 2\sigma\dot{w}, \tag{2c}$$

$$w = u\left(x_c,\ t\right) - v, \tag{2d}$$

where $\rho(x)$ is the material density of the beam, and $D(x) = E(x)I(x)$ is the bending stiffness, $p = p(x,t)$ stands for the pointwise external force induced at the position $x = x_F$. The force $f = f(x,t)$ is the restoring force of the oscillator written in form of the relative motion $w = u\left(x_c,\ t\right) - v$. The mass ratio ϵ defined by $\epsilon = m/m_{beam}$ is supposed to be small (m is the mass of the absorber and m_{beam} is the total mass of the beam). As for the boundary conditions, the beam is considered to be clamped at $x = 0$ and free at $x = L$.

The damping induced by the viscoelastic layer is modelled with the Ross-Kerwin-Ungar method [2], in which a complex bending stiffness $D^*(x)$ is introduced and can be expressed as,

$$D^*\left(x\right) = \begin{cases} E_b I_b(x)\left(1 + j\eta_b\right), & \forall x \in [0, x_{abh}], \\ E_b I_b(x)\left[\left(1 + j\eta_b\right) + \dfrac{E_l}{E_b}\left(\dfrac{h_l}{h_b(x)}\right)^3\left(1 + j\eta_l\right) + \right. & \\ \left. \dfrac{3\left(1 + \frac{h_l}{h_b(x)}\right)^2 \frac{E_l h_l}{E_b h_b(x)}\left(1 - \eta_b\eta_l + j\left(\eta_b + \eta_l\right)\right)}{1 + \frac{E_l h_l}{E_b h_b(x)}\left(1 + j\eta_l\right)}\right], & \forall x \in [x_{abh}, L], \end{cases} \tag{3}$$

where j is the imaginary unit, E_b, I_b, and η_b stand respectively for the bending stiffness, the Young's modulus, the moment of inertia and the loss factor of the beam alone, while E_l and η_l are the Young's modulus and the loss factor of the viscoelastic layer. In addition, a modification on the thickness $h(x) = h_b(x) + h_l$ and material density $\rho(x) = \left(\rho_b h_b + \rho_l h_l\right)/h$ at the ABH area are also performed due to the added mass of the damping layer.

A modal approach, whose implementation details are given in [6], is applied to numerically solve the problem described in 2 in the time domain. A special emphasize on the added new dof introduced by the nonlinear damper will be further explained here. First of all, the beam displacement is written as $u(x,t) = \sum_{k=1}^{N_m} \phi_k(x) q_k(t)$, where $q_k(t)$ is the modal

coordinate associated to mode $\phi_k(x)$, and N_m is the number of modes kept in the expansion. Introducing the modal expansion into (2), and projecting the dynamics onto each mode yields :

$$\ddot{q}_k + 2\xi_k\omega_k\dot{q}_k + \omega_k^2 q_k = p\phi_k\left(x_F\right) - f\phi_k\left(x_c\right), \tag{4a}$$

$$m\ddot{v} = f, \tag{4b}$$

$$f = k_l w + k_n w^3 + 2\sigma\dot{w}, \tag{4c}$$

$$w = \sum_{k=1}^{N_m} q_k\phi_k\left(x_c\right) - v, \tag{4d}$$

where ω_k and ξ_k are respectively the eigenfrequency and the the modal damping ratio associated to each mode k. Hence, the original problem with PDE is transferred to a set of ODEs with time variables only. Before solving Eqs. (4), a eigenvalue problem should be solved to determine $\phi_k\left(x\right)$, ω_k, and ξ_k for each mode. Such eigenvalue problem is written from Eq. (2a), considering that $f = p = 0$. A finite difference method with a non-uniform grid is applied to discretize the variable thickness of the ABH beam. All the complete details are given in [2]. They are skipped here for conciseness. Once the eigenvalue problem solved, the last step of the numerical model consists in the time integration of Eqs. (4). It is done using the exact energy conserving numerical scheme developed in [17].

Let $t_n = n\Delta t$, with n the step index and Δt the time step. The specific feature of the numerical integrator developed in [17] is to use the modal approach for the linear part, whereas the contact force are computed in the physical space. To that purpose, the relationship between the modal space and the physical space needs to be explicited. We introduce $\mathbf{S}_F = \left[\phi_1\left(x_F\right),\ \phi_2\left(x_F\right),\ \cdots,\ \phi_{N_m}\left(x_F\right)\right]$, as the modal matrix containing the first N_m beam modes at x_F , and $\mathbf{S}_c = \left[\phi_1\left(x_c\right),\ \phi_2\left(x_c\right),\ \cdots,\ \phi_{N_m}\left(x_c\right)\right]$ the modal matrix at point x_c. The relationship with the modal expansion allows one to write $u\left(x_c, n\Delta t\right) = \mathbf{S}_c\mathbf{q}$, and $u\left(x_F, n\Delta t\right) = \mathbf{S}_F\mathbf{q}$. With these definitions, Eqs. (4) can then be written at each time step n as:

$$\mathbf{q}^{n+1} = \mathbf{C}\mathbf{q}^n - \tilde{\mathbf{C}}\mathbf{q}^{n-1} + \Delta t^2\left(\mathbf{S}_F^T p^n - \mathbf{S}_c^T f^n\right), \tag{5a}$$

$$m\delta_{t\cdot}v^n = f^n, \tag{5b}$$

$$f^n = k_l w^n + k_n (w^n)^2 \mu_{t\cdot} w^n + 2\sigma\delta_{t\cdot}w^n, \tag{5c}$$

$$w^n = \mathbf{S}_c\mathbf{q}^{\mathbf{n}} - v^n. \tag{5d}$$

where p^n and f^n are respectively the external and restoring forces at time step n. The matrices $\mathbf{C}$ and $\tilde{\mathbf{C}}$ are two diagonal matrices whose expressions could be found in [17], $\delta_{t\cdot}$ is a centred time difference reading $\delta_{t\cdot}w^n = \left(w^{n+1} - w^{n-1}\right)/2\Delta t$, and $\mu_{t\cdot}$ is an averaging operator: $\mu_{t\cdot}w^n = \left(w^{n+1} + w^{n-1}\right)/2$. The advantage of this particular choice stems from the consideration of ensuring the energy conserving properties and avoid numerical dispersion. It should be noted that before the numerical analysis, a convergence study should first be performed on the sampling frequency $F_s = 1/\Delta t$ and the number of modes N_m, in order to appropriately select the numerical parameters. It was demonstrated that an arrangement with $N_m = 20$ and $F_s = 16$kHz is sufficiently enough for obtaining accurate results in our studies.

Nonlinear dampers attached to a uniform beam

The first results and comparisons of the three selected methods (TMD, NES and BNES) have been first tested numerically on a simply supported uniform beam. goal is here to suppress one targeted single resonance of the beam using each of the three selected methods. Fig. 2 provides two simulation results: 1/ the optimization of the nonlinear cubic stiffness k_c and the location x_c of a NES is performed using the energy dissipation E_{diss} cost function (see Fig. 2(a)). 2/ The performance of the system subjected to a harmonic excitation at the circular frequency ω_F in the vicinity of the fundamental frequency of the beam ω_1 is illustrated in Fig. 2(b).

It can be seen that with a appropriate design, each strategy, either a TMD, a NES, or a BNES can effectively suppress the resonance peak of the beam which confirms their efficiency. For the next step, the three methods will then be applied to the ABH beam in order to improve the low frequency performance, with comparisons and optimizations for each of the three mentioned method.

Nonlinear dampers attached to an ABH beam

Parameters of the ABH beam and linear performance

The geometrical and material parameters for the selected ABH beam used in our simulations are listed in Table 1. These choices are related to the experimental beam used in the previous works in[2]. The first line in Table 1 defines also a uniform beam of constant thickness, which will be used subsequently as reference in order to draw out comparisons.

The driving mobility defined as the ratio between the velocity spectrum and the input force spectrum at x_F, is compared in Fig. 3 between the reference (naked) beam and the ABH beam. It could be found that the ABH effect is particularly noticeable on the high-frequency part of the mobility. The cut-on frequency of the ABH effect is evaluated at $f_c = 500$ Hz,

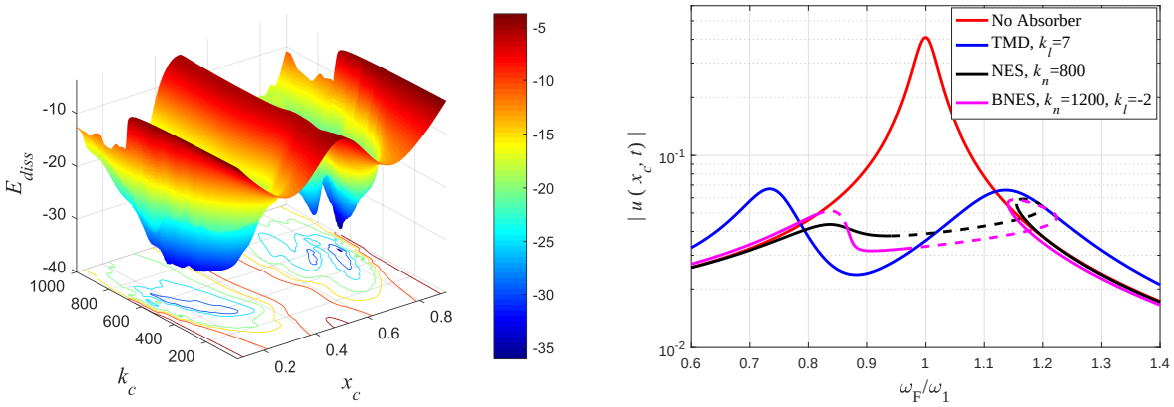

(a) (b)

Figure 2: (a): Dissipated Energy E_{diss} of a NES having a purely nonlinear cubic stiffness k_c and located at x_c. (b): Frequency response of the beam under a harmonic excitation in the vicinity of the first resonance frequency ω_1. Comparisons among the optimized TMD, NES and BNES configurations, with the same damping $\sigma = 0.1$. $|u(x_c,t)|$ refers to the beam displacement at the attached point, the dashed lines indicate that the periodic solution is unstable.

Beam parameters	ABH profile	viscoelastic layer
L=80cm	x_{abh}=71cm	h_l=400μm
h_0=4mm	x_{end}=80.685cm	E_l=10Mpa
b=2cm	h_t=20μm	ρ_l=1000 kg $\cdot$ m^3
E_b=70Gpa		η_l=160%
ρ_b=2700kg $\cdot$ m^3		
η_b=0.2%		

Table 1: Geometrical and material parameters selected for the studied ABH beam.

above which excellent damping properties in the ABH beam with strong attenuation of the sharp resonance peaks (more than 20dB) could be observed. However, at the frequency range below 500Hz, sharp resonance peaks still exist, the ABH almost has no effect. Therefore, in the next sections, our goal will be to improve the damping properties of the ABH effect in the frequency range $[0, 500]$ Hz, by associating the ABH with a special vibration absorber: TMD, NES or BNES.

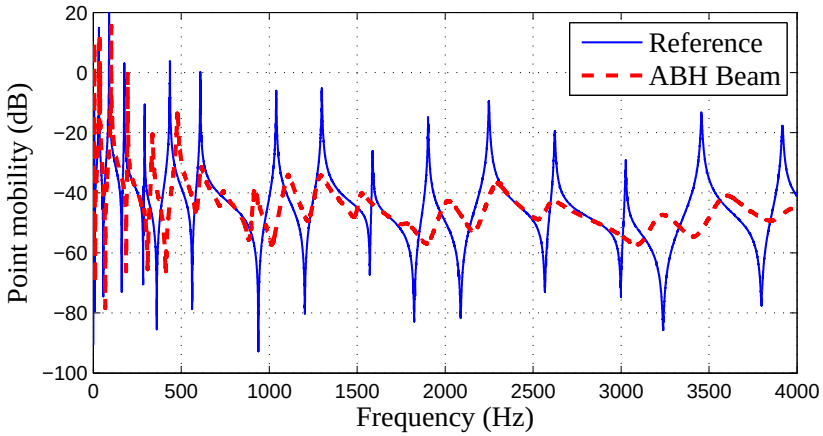

Figure 3: Comparison of the driving mobilities of the ABH and the uniform beam given in Table 1. Excitation and measurement point are fixed at $x_F = 24$ cm. The excitation is a white noise excitation on $[0, 5000]$ Hz, with amplitude 1 N.

Effect of vibration absorbers on ABH beam

To investigate in the effect of the adding vibration absorber on the performance of the ABH beam, a white noise excitation in the frequency band $[0, 500]$ Hz is considered. Four different cases including the ABH beam without damper (the reference case), the ABH with an attached TMD, the ABH coupled to a NES with pure cubic stiffness, the ABH coupled to a BNES with both cubic stiffness and negative linear stiffness, are then discussed and compared. Fig. 4 shows the output velocity spectrum at the excitation point for each case. Clearly enough, each method could be able to reduce the resonant responses in the targeted low frequency range, while for this typical simulation, the performance is significant for the first 4 modes but less important for the others. More precisely, for mode 2, a 15-25dB reduction could be observed,

and for mode 3, this reduction is around 10-20dB. Thus, by using a linear or nonlinear absorber, the average performance of the ABH beam at the low frequency range is considerably improved. On the other hand, the spectra above the 500Hz indicate that while not significant, the nonlinearity of the NES and BNES brings some transfer of the energy from the low frequency to the high frequency, whereas the TMD shows a linear behaviour without such energy transfer.

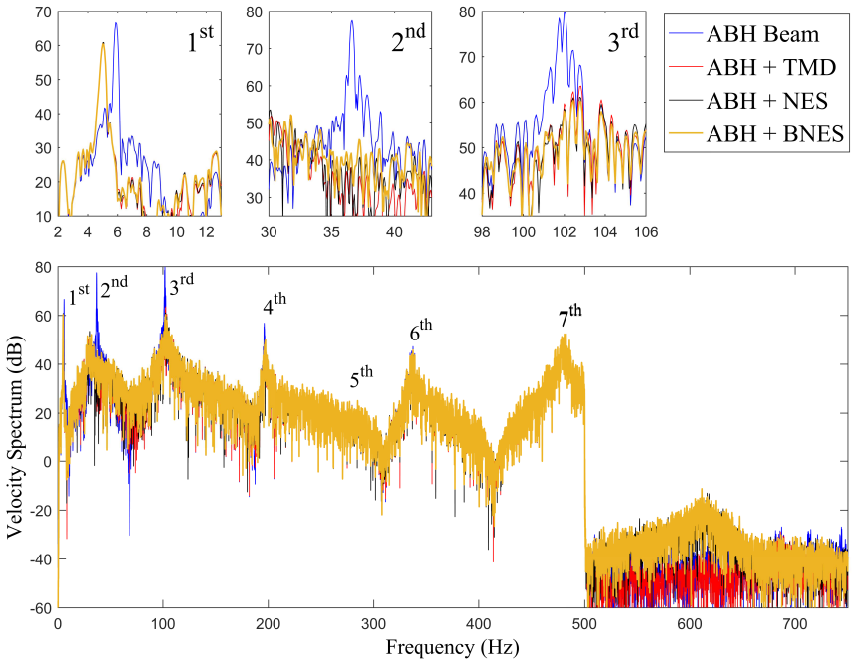

Figure 4: Reduction of the resonance peaks of an ABH beam by using a TMD with $k_l = 800$ N/m, a NES with $k_n = 3 \times 10^9$ N/m^3, and a BNES with $k_l = -300$ N/m, $k_n = 3 \times 10^9$ N/m^3. For all cases, $\sigma = 0.5\text{N} \cdot \text{s/m}$, $x_c = 0.72$ m. The beam is excited with a white noise of $[0, 500]$ Hz, with an amplitude $A = 5$ N and a location $x_F = 0.24$ m. The dynamics are simulated up to 10s.

A performance indicator is proposed for a more quantitative comparison :

$$I = 10\log_{10}\left(\frac{\int_{f_0}^{f_{end}} V_c^2 \,\mathrm{d}f}{\int_{f_0}^{f_{end}} V_{ref}^2 \,\mathrm{d}f}\right), \tag{6}$$

where V stands for the power spectrum of velocity at the exciting point, with subscript c or ref referring respectively to the current case and the reference case (*i.e.* the ABH beam without attachment). This indicator allows one to assess the improvements brought by each method over an arbitrary frequency band $[f_0, f_{end}]$. Having in mind the purpose that we want to compare the performances of the three vibration absorbers in the low frequency range below the cut-on freuqency of the ABH, some useful indicators can thus be defined in Tab. 2. Here, I_{ω_1} to I_{ω_3} are the indicators quantifying the reduction in the vicinity of each eigenfrequencies ω_1 to ω_3, while I_{ave} provides an evaluation for the average performance at the low frequency band $[0,\ 500]$ Hz of the ABH beam.

Indicators	I_{ω_1}	I_{ω_2}	I_{ω_3}	I_{ave}
$\omega_i/2\pi$ (Hz)	5.9	36.7	101.9	/
$[f_0,\ f_{end}]$ (Hz)	[0, 15]	[30, 45]	[95, 110]	[0, 500]

Table 2: Frequency bands used for defining the performance indicators

The performance indicators for all the cases considered in Fig. 4 are reported in Fig. 5. Considering the fact that the chosen excitation signal is random, a single simulation result may not give an accurate value for the indicators, hence a average values over 20 random selections for each indicator I_{ω_1} to I_{ave}, together with the standard variations is depicted in Fig. 5. One can see that the variations brought by the randomness of the excitation is significant. For I_{ω_1}, a worst fluctuation at around $\pm$6dB is observed. At the higher frequencies , the indicators are less prone to variations. As a result, there finally exists a variation at around $\pm$1.5dB for the average performance I_{ave}. Thus, a single simulation is not sufficient enough to provide accurate values for each indicator. A Monte Carlo method for obtaining convergence results has then been performed. It is shown that, by make the average value of at least 5 times of simulation samples, I_{ave} can be converged to to a very small variation of less than 0.2dB. In this paper hereafter, for each case, we will repeat 10 times each simulation, and we will take the average value for computing the indicators.

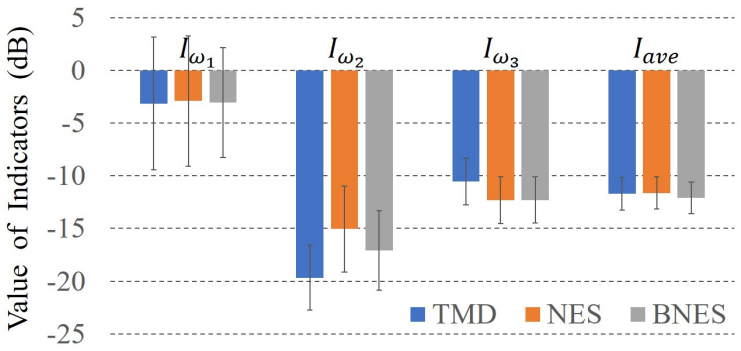

Figure 5: Histograms of indicators I_{ω_1} to I_{ave} calculated for the four cases given in Fig. 4. Average values and standard deviation are computed from 20 randomly generated white noise excitations with amplitude 5N and frequency band $[0, 500]$Hz.

It should be emphasized that the parameters associated to each method are randomly selected, hence their performances are not really optimized currently but discussed thanks to the help of the indicators. It allows to propose some guidelines for an optimal design.

Tuning the vibration absorbers: parametric study

This section is devoted to the parametric tuning and the optimization of the different vibration absorbers. The interested parameters are the linear and nonlinear stiffnesses k_l and k_n, the damping coefficient σ, and the location x_c. For all the simulations, the external force is a white noise excitation limited to the low frequency band $[0, 500]$Hz, with amplitude $A = 5$N and location $x_F = 0.24$m.

Since the linear and nonlinear stiffnesses play an important role in the energy transfer between the ABH and the vibration damper, their effects are first investigated. Fixing x_c=0.72m, σ=0.5Ns/m, and $\epsilon = 0.1$ and varying k_l and k_n, the values of different indicators are depicted in Fig. 6 for the three vibration absorbers.

As the linear stiffness k_l in the TMD increases, I_{ω_1}, I_{ω_2}, I_{ω_3}, and I_{ave} show a similar trend, with different minimum values for each indicator (see Fig. 6(a)). For example, I_{ω_1} meets its optimal value of $I_{\omega_1} = -15$dB for $k_l = 20$N/m, showing that the best reduction is obtained for the resonance peak of the first mode. For I_{ω_2} and I_{ω_3}, the optimal stiffnesses are $k_l = 500$N/m and $k_l = 5000$N/m, respectively. Each optimal stiffness is just consistent with the eigenfrequency of the correspond mode, which is also the key rule in the classical frequency tuning of TMD. Nevertheless, the combined effects reported by the average indicator I_{ave} show that a global minimum can be found for k_l around 1000N/m.

For the case of an attached NES, trends similar to the TMD case can be observed (see Fig. 6(b)). The optimal performance for the reduction of the resonance peaks of modes 1-3 could be found respectively for $k_n = 10^7\mathrm{N/m}^3$, $k_n = 10^9\mathrm{N/m}^3$, and $k_n = 3 \times 10^{10}\mathrm{N/m}^3$, with indicators respectively equal to I_{ω_1}=-15dB, I_{ω_2}=-23dB, I_{ω_3}=-20dB. Besides, for the average performance, $k_n = 2 \times 10^9\mathrm{N/m}^3$ gives the optimal tuning.

In Fig. 6(c-d), the effect of the negative stiffness k_l shows quite different trends for different values of k_n. For a relatively small value of $k_n = 10^6\mathrm{N/m}^3$, the effect of varying k_l is important. The optimal performance can be easily observed for each single mode 1-3 as $k_l = -10\mathrm{N/m}$, $k_l = -300\mathrm{N/m}$, and $k_l = -2000\mathrm{N/m}$ respectively, and the optimal average performance is obtained within $k_l \in [300, 500]$ N/m. However, for higher values of k_n, for example $k_n = 2 \times 10^9\mathrm{N/m}^3$ (see Fig. 6(d)), where the nonlinear stiffness has been tuned to the optimal value found for the pure cubic NES, the effect of k_l become much less noticeable: varying k_l does not bring an evident improvement and the indicators remain stable on a wide range of k_l. In this case, the dynamical behaviour is dominated by the nonlinear stiffness. Consequently, the effect of having a (now small) linear negative stiffness is negligible and the dynamics of the damping mechanism is dominated by that of a classical NES with targeted energy transfer. Finally, as testified by the abrupt increase of I_{ave} for $k_l < -1000$, one can remark that when the negative linear stiffness becomes too large, the performance is largely reduced.

The influence of the damping σ on the performance of each vibration damper is depicted in Fig. 7. In each case, as damping increases, the performance improves at first and then decreases, hence for effective vibration suppression, neither too large nor to small value of damping is appropriate. This conclusion could be explained by the fact that when the damping is too small, the absorber might be insufficient to damp out the energy, while an inappropriately too large value on the other hand reduces also the relative motion the energy transfer between the beam and the absorber becomes more difficult. As a result, a damping coefficient of $\sigma = 3\ \mathrm{N \cdot s/m}$ could be selected for the best suppression. Note the difference among the absorbers, one can conclude that at low damping level, NES and BNES generally show a much better behaviour than the TMD due to their strong nonlinearity. However, the difference becomes less significant when the damping increases up to $\sigma = 1\ \mathrm{N \cdot s/m}$, since overdamped motions make it more difficult for the NES and BNES to activate their nonlinearity and take advantage of it.

Varying the location of the vibration absorbers on the ABH beam, the performance indicator I_{ω_2} of mode 2 as a function of x_c is depicted in Fig. 8(a), for each of the three tested configurations: TMD, NES and BNES. Interestingly, a direct link between on the value of I_{ω_2} and the corresponding mode shape function is observed, whatever the absorber is mounted on the ABH beam. This point is verified by the fact that the absolute value of the mode function $|\phi_2(x)|$, when multiplied

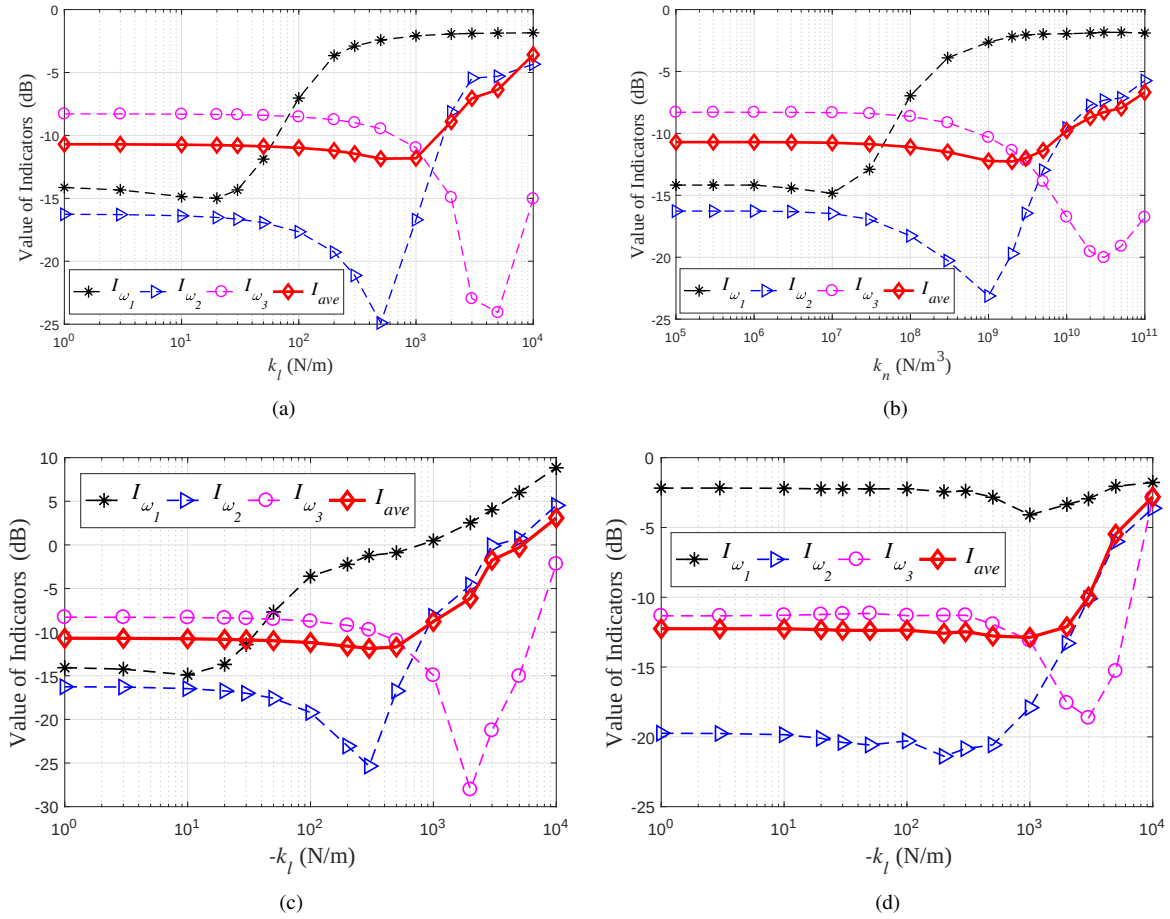

Figure 6: Variations of indicators I_{ω_1}, I_{ω_2}, I_{ω_3}, and I_{ave} as functions of the linear and nonlinear stiffnesses: (a) TMD, indicators as function of linear stiffness k_l (b) NES, indicators as function of the nonlinear stiffness k_n, (c) BNES, indicators as function of the negative stiffness $-k_l$, with nonlinear stiffness fixed as $k_n = 10^6$ N/m^3, (d) BNES, indicators as function of the negative stiffness $-k_l$, with $k_n = 2 \times 10^9$ N/m^3.

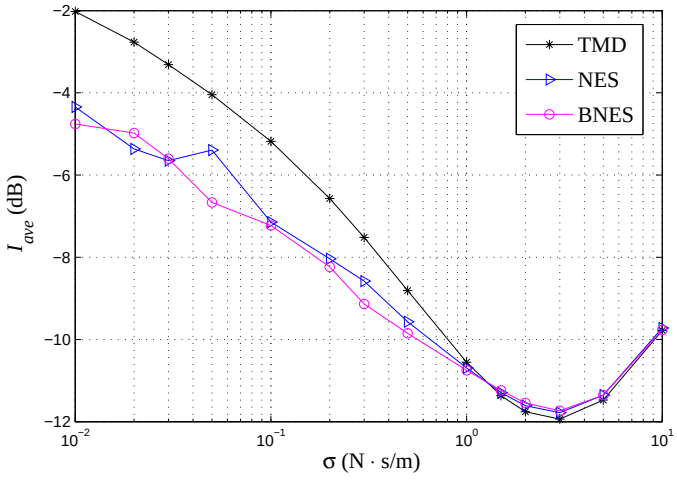

Figure 7: Effect of the damping coefficient σ on the indicator I_{ave}. The TMD Stiffness is $k_l = 500$N/m, the NES Stiffness $k_n = 2 \times 10^9$N/m^3, and the BNES Stiffnesses are $k_n = 2 \times 10^9$N/m^3, $k_l = -300$N/m. For all the absorbers, the mass ratio is ϵ=0.1

by a certain coefficient, is well fitted with the variation of the indicator I_{ω_2}. Hence, as an direct conclusion, in order to obtain an optimal reduction of a given mode, the linear or nonlinear dampers should be located at a local maximum of the given mode described by the shape function.

Considering the combined effects of the low frequency modes involved below the cut-on frequency, the value of average performance indicator I_{ave} exhibits the variation depicted in Fig. 8(b). For all the absorbers, the optimal location lies clearly in the ABH termination (gray area) of the beam, where most of the vibration is localized. However, for practical considerations, one should keep in mind also that in this ABH area, the thickness of the ABH severely decrease from

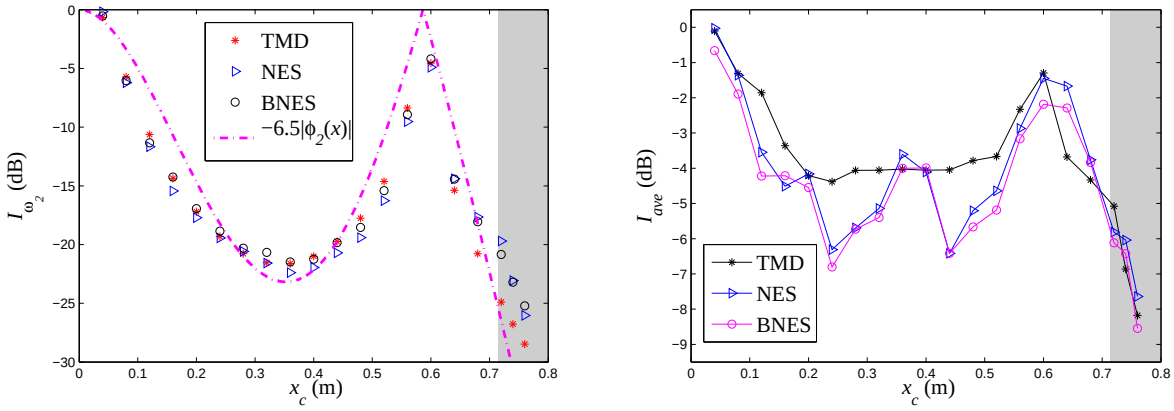

(a) (b)

Figure 8: Effect of the position x_c of the absorbers on the values of the performance indicators. TMD stiffness is $k_l = 500$N/m, NES stiffness $k_n = 2 \times 10^9 \mathrm{N/m^3}$, and BNES stiffnesses are $k_n = 2 \times 10^9 \mathrm{N/m^3}$ and $k_l = -300$N/m, (a): value of I_{ω_2}, (d): value of I_{ave}. The damping for each vibration damper is selected as $\sigma = 0.5\mathrm{N \cdot s/m}$ for (a) and $\sigma = 0.05\mathrm{N \cdot s/m}$ for (b). The gray area refers to the ABH profile.

$x = 0.71$m in the selected design. Consequently, for practical reasons it does not appear as desirable to set a damper in this region of small thickness where the beam is weaker. On the region on constant thickness, there are also two optimal positions clearly observed for the NES and BNES, at $x_c = 0.24$m and $x_c = 0.44$m. While the TMD shows a quite flat plateau at a wider range $x \in [0.2, 0.55]$m, and is not able to produce averaged improved performance below -4dB. This important difference also shows that the nonlinear absorbers are more sensitive to the location as compared to the TMD.

Robustness to the forcing amplitude

The last parameter to be studied is the forcing amplitude. Indeed, as it is expected, the influence of this parameter is crucial for the cases of a NES ad a BNES. It is well known that unlike a linear system, a nonlinear system has quite different performance at different energy levels, hence a NES or BNES that is optimally designed at one energy level might loses its effectiveness at another energy level, and vice versa. On the other hand, for a NES, an energy barrier exists for activating targeted energy transfer, making the NES generally not able for effective vibration suppression in too small vibration amplitudes, while a BNES is known to have a smaller energy barrier. Thus the effect of forcing amplitude becomes to be of special significance for evaluating the performance of these vibration absorbers.

For forcing amplitude A increases from 0.01 to 100N, the variations of I_{ω_2} and I_{ave} are shown in Fig. 9. The performances of TMD (black), NES (blue) and BNES (red) are then compared for two different values of parameters, where the solid lines refers to the case where the optimal parameters in each strategy, while the dashed lines show how they behave in a weak damping case with internal damping $\sigma = 0.05$. Indeed, it has appeared interesting to show this case since the optimal damping value is very large and probably difficult to implement in a practical situation.

Major differences could be found for the three absorbers on the effect of forcing amplitude. As it can be expected, the TMD is always independent to the amplitude: the indicator at all excitation level remains the same. On the other hand, the performances of the NES or the BNES are highly relevant to the amplitude, in Fig. 9(a), a energy barrier at 0.1N could be observed for the NES. Below this barrier, the performance of I_{ω_2} is weak and it starts to increase to meet an optimal performance around 2.5N. The performance is deteriorated at very large amplitudes. Similar conclusion is also evidenced for the average performance I_{ave} in Fig. 9(b). When adding a negative stiffness in the NES, representing a BNES, the performance at the low amplitude level that limited by the energy barrier is improved. Finally, at very high excitation level, the performance of NES and BNES are similar, and both ineffective.

In a summary all these results show that all the proposed solutions, if appropriately designed and tuned, are able to achieve a clear broadband vibration mitigation.

Conclusion

Aiming at improving the low frequency performance of a beam equipped with an ABH termination three different types of vibration absorbers (TMD, NES and BNES) have been proposed and simulated numerically. The main results confirm that all the proposed vibration absorbers, despite being linear or nonlinear, once appropriately designed, could be effective to reduce the low frequency resonance peaks in the ABH beam with a reduction at more than 10dB.

The parametric effect in each method is also discussed. The values of the stiffnesses (linear and non-linear) play the most important role for the performance of each absorber and it should be carefully designed according to different applications. On the other hand, at weak damping level, NES and BNES outperform the TMD, but for large values of the damping, they behaves linearly and all the three absorbers exhibit similar performances. The investigation on the location illustrates that whatever the absorber is, its optimal performance for a single resonance modes lies in the local maximum of the targeted

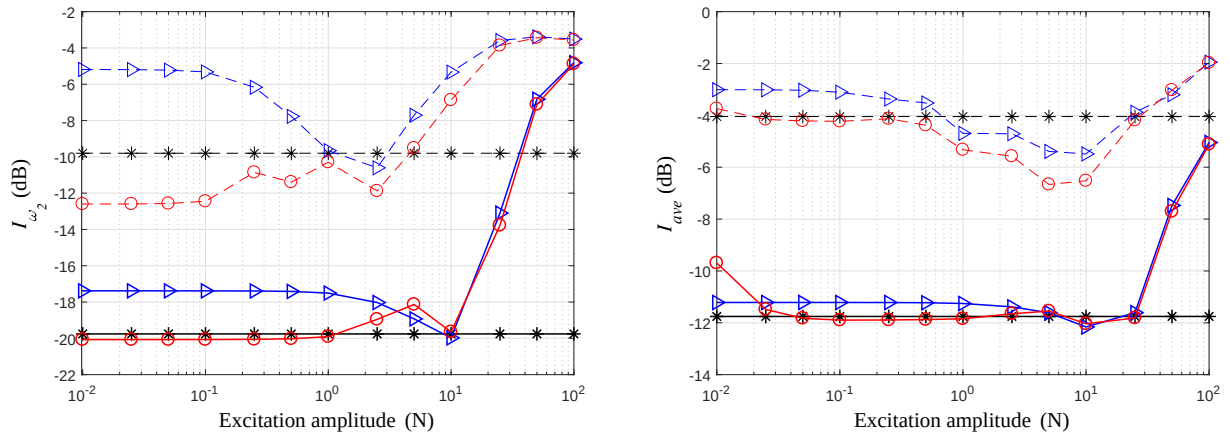

Figure 9: Robustness of the performance indicators according to the forcing amplitude, (a): value of I_{ω_2}, (b): value of I_{ave}. Solid line: computation with the optimal parameters, dashed line: comparison in the weak damping case. dashed black: TMD with $k_l = 500$N/m and weak damping $\sigma = 0.05\text{N} \cdot \text{s/m}$; solid black: TMD with optimized parameters $\sigma = 2\text{N} \cdot \text{s/m}$ and $k_l = 500$N/m; dashed blue: NES with $k_n = 2 \times 10^9 N/m^3$ and weak damping $\sigma = 0.05\text{N} \cdot \text{s/m}$; solid blue: NES with optimized parameters $\sigma = 2\text{N} \cdot \text{s/m}$ and $k_n = 2 \times 10^9 N/m^3$; dashed red: BNES with $k_n = 2 \times 10^9 N/m^3$, $k_l = -300$N/m, and weak damping $\sigma = 0.05\text{N} \cdot \text{s/m}$; solid red: BNES with optimized parameters $\sigma = 2\text{N} \cdot \text{s/m}$, $k_l = -300$N/m, and $k_n = 2 \times 10^9 N/m^3$;

mode function.

A Robustness study to the forcing amplitude demonstrates that while a TMD with linear behavior is always independent on the vibration level, the NES and BNES could be strongly dependent on the forcing amplitude. A NES is generally effective only at a moderate excitation level, and its performance is deteriorated at low and high amplitude levels. Hence for a robustness point of view, a TMD is better than the NES. Using a BNES improves a lot the performance at low amplitude level, but the performance at high amplitude level stays also ineffective.

References

[1] V.V. Krylov, F.J.B.S. Tilman, Acoustic 'black holes' for flexural waves as effective vibration dampers, Journal of Sound and Vibration, 2004, **274**(3-5): 605-619.

[2] V. Denis, A. Pelat, F. Gautier, B. Elie, Modal overlap factor of a beam with an acoustic black hole termination, Journal of Sound and Vibration, 2014, **333**, 2475-2488.

[3] J. Leng, V. Romero-García, A. Pelat, R. Picó, J-P. Groby, F. Gautier, Interpretation of the Acoustic Black Hole effect based on the concept of critical coupling, Journal of Sound and Vibration, 115199, 2020.

[4] O. Aklouche, A. Pelat, S. Maugeais, F. Gautier, Scattering of flexural waves by a pit of quadratic profile inserted in an infinite thin plate, Journal of Sound and Vibration, 2016, **375**, 38-52.

[5] V. Denis, A. Pelat, C. Touzé, F. Gautier. Improvement of the acoustic black hole effect by using energy transfer due to geometric nonlinearity, International Journal of Non-Linear Mechanics,2017, **94**:134-145.

[6] H. Li , C. Touzé, A. Pelat, F. Gautier and X. Kong, A vibro-impact acoustic black hole for passive damping of flexural beam vibrations, Journal of Sound and Vibration, 2019, **450**, 28-46.

[7] J. D. Hartog, Mechanical Vibrations, McGraw-Hill, New-York, 1934.

[8] C. Lee, Y. Chen, L. Chung, Y. Wang, Optimal design theories and applications of tuned mass dampers, Engineering Structures, 2006, **28**(1): 43-53.

[9] S. Krenk and J. Høgsberg, Tuned mass absorber on a flexible structure. Journal of Sound and Vibration, 2014, **333**(6): 1577-1595.

[10] M. Parseh, M. Dardel and M. H. Ghasemi, Performance comparison of nonlinear energy sink and linear tuned mass damper in steady-state dynamics of a linear beam, Nonlinear Dynamics, 2015, **81**(4): 1-22.

[11] Y. S. Lee, A. F. Vakakis, L. A. Bergman, L.A., D. M. McFarland, G. Kerschen, F. Nucera, S. Tsakirtzis and P. N. Panagopoulos, Passive non-linear targeted energy transfer and its applications to vibration absorption: a review. Proceedings of the Institution of Mechanical Engineers, Part K, Journal of Multi-body Dynamics, 2008, **222**(2): 322-329.

[12] O. V. Gendelman, Y. Starosvetsky, and M. Feldman, Attractors of harmonically forced linear oscillator with attached nonlinear energy sink , part I: description of response regimes, Nonlinear Dynamics, 2008, **51**(1-2): 31-46.

[13] O. V. Gendelman, Y. Starosvetsky and M. Feldman, Attractors of harmonically forced linear oscillator with attached non- linear energy sink, part II: optimization of a nonlinear vibration absorber, Nonlinear Dynamics, 2008, **51**(1-2): 47-57.

[14] F. Georgiades and A. F. Vakakis, Dynamics of a linear beam with an attached local nonlinear energy sink, Communications in Nonlinear Science and Numerical Simulation, 2007, **12**(5), 643-651.

[15] G. Habib and F. Romeo, The tuned bistable nonlinear energy sink. Nonlinear Dynamics, 2017, **89**(1):179-196.

[16] D. Qiu, T. Li, S. Seguy, and M. Paredes, Efficient targeted energy transfer of bistable nonlinear energy sink: application to optimal design. Nonlinear Dynamics, 2018, **92**(2):443-461.

[17] C. Issanchou, S. Bilbao, J.L. Le Carrou, C. Touzé, and O. Doaré. A modal-based approach to the nonlinear vibration of strings against a unilateral obstacle: Simulations and experiments in the pointwise case. Journal of Sound and Vibration, 2017, **393**:229-251.